

Submitted to Astronomical Journal; revised 7/12/05

# The Properties of Intergalactic C IV and Si IV Absorption, I: Optimal Analysis of an Extremely High S/N Quasar Sample

Antoinette Songaila<sup>1</sup>

*Institute for Astronomy, University of Hawaii, 2680 Woodlawn Drive, Honolulu, HI 96822*

acowie@ifa.hawaii.edu

## ABSTRACT

We have analyzed the properties of metals in the high redshift intergalactic medium using a novel objective pixel optical depth technique on a sample of extremely high signal-to-noise Keck HIRES and ESI spectra of 26 quasars between redshifts 2.1 and 6.4. The technique relies on using the doublet nature of the common ions C IV and Si IV that are the principal metal tracers in the intergalactic medium outside of the Ly $\alpha$  forest. Optical depths are statistically corrected for contamination by other lines, telluric absorption, bad pixels, continuum fitting, etc. and for incompleteness, and we achieve in this way an increased sensitivity of approximately 0.5 dex over previous analyses. As with existing pixel optical depth analyses, the method is completely objective and avoids subjective cloud selection and Voigt profile fitting, but, unlike existing techniques, we do not compare the ion optical depths with H I optical depths to determine the ion optical depth distributions; we therefore avoid problems arising from different velocity widths in the ion and H I. We have shown how the conventional analysis can be reproduced using a percolation method to generate pseudo-clouds from ion optical depths. Using this set of pseudo-clouds, we have generated C IV column density distributions and have confirmed that the shape of the C IV column density distribution remains essentially invariant, with slope  $-1.44$ , from  $z = 1.5$  to  $z = 5.5$ . This in turn confirms the lack of redshift evolution of  $\Omega(\text{CIV})$  for  $z = 2$  to  $z = 5$ , both for all absorbers with column density,  $\log N = 12 - 15$  and for stronger absorbers with  $\log N = 13 - 14$ . The generation of pseudo-clouds from

---

<sup>1</sup>Visiting astronomer, W. M. Keck Observatory, jointly operated by the California Institute of Technology and the University of California.

the optical depth vectors also gives information on the column density environment of a given optical depth. We find that for the higher resolution HIRES data there is a tight relation,  $\tau \sim N^{0.7}$ , between the peak optical depth and the column density. We have then analyzed the ion redshift evolution directly and model-independently from the optical depth vectors themselves and show that there is little evolution in the total amount of C IV from  $z = 2$  to  $z = 5$ , though there is a turndown of at least a factor of two in  $\Omega(\text{CIV})$  above  $z = 5$ . We do, however, see substantial evolution in the ratio, Si IV/C IV. In two subsequent papers in the series, we will use this technique to investigate what fraction of the absorbers lie in galactic wind outflows (Paper II) and what metallicity is associated with regions of  $\tau(\text{Ly}\alpha) < 1$  (Paper III).

*Subject headings:* early universe — intergalactic medium — quasars: absorption lines — galaxies: formation

## 1. Introduction

The availability of very efficient high-resolution spectrographs on 8–10 meter class telescopes (Vogt et al. 1994, d’Odorico et al, 2000) provided the very high S/N observations of high redshift quasars needed to confirm earlier suggestions (e.g. Meyer & York 1987) that many of the stronger lines seen in the Lyman alpha forest of quasar spectra have associated metal absorption lines (Cowie et al. 1995, Tytler et al. 1995). Over the past few years these metal features have been extensively studied using Voigt profile fitting (e.g. Songaila & Cowie 1996; Songaila 1998; Ellison et al. 2000; Songaila 2001; Pichon et al. 2003; Simcoe, Sargent & Rauch 2004; Aracil et al. 2004) and the so-called pixel optical depth (POD) methods in which the metal-line optical depths are cross-correlated with neutral hydrogen absorption (Cowie & Songaila 1998; Songaila 1998; Aguirre, Schaye & Theuns 2002; Schaye et al. 2003; Aguirre et al. 2004). Down to the sensitivity limit of these methods ( $\tau(\text{Ly}\alpha) \sim 1$ ) metal enrichment seems ubiquitous, with a median value of  $[\text{C}/\text{H}] = -3.47$  at an overdensity of  $10^{0.5}$ , though there is a considerable spread of nearly a dex in the metallicity at every overdensity and an equally significant trend with overdensity (Schaye et al. 2003). It also appears that there is very little change in the distribution of C IV absorbers over a very wide redshift range (Songaila 2001).

The origin of these metals is still unclear: some may be in the process of being injected into the IGM from galaxies at the redshifts in question (we refer to this as contemporary injection) (Adelberger et al. 2003, Pettini et al. 2003), whereas others may have been put in place by earlier galaxy formation or by generations of population III stars (Wasserburg

& Qian 2000; Madau, Ferrara & Rees 2001; Qian, Sargent & Wasserburg 2002; Bromm, Yoshida & Hernquist 2003; Venkatesan & Truran 2003; Mackey, Bromm & Hernquist 2003; Fujita et al. 2004; Daigne et al. 2004; Yoshida, Bromm & Hernquist 2004). It is very likely that both processes contribute, and one of the primary goals of the present series of papers is to see if we can distinguish among systems formed by the various processes and determine if the enrichment mechanism relates to intrinsic properties of the metal systems such as their column density, velocity structure, or redshift.

An essential prerequisite of these analyses is, however, the existence of extremely high signal-to-noise observations of the quasars. Over the past years we have been obtaining very long-exposure spectra of the brightest quasars accessible with the HIRES and ESI spectrographs on the Keck 10-m telescope. In this set of papers we describe these observations and then use them to reanalyse the properties of the forest metals. In this first paper we describe a more objective technique for analyzing the spectra which allows us to make a deeper analysis of the data than is possible with Voigt profile fitting. In two subsequent papers we will use this method to address two of the outstanding problems associated with IGM metal enrichment scenarios, namely what fraction of the absorbers lie in galactic wind outflows (Paper II) and what metallicity is associated with regions of Lyman alpha optical depth,  $\tau(\text{Ly}\alpha) \leq 1$  (Paper III).

Voigt profile fitting is an inherently subjective procedure, both in the initial visual selection of the line candidates and also in the choice of cloud model to fit the line. The errors and incompleteness are therefore hard to quantify. The current POD methods, while extremely sensitive and objectively quantifiable, are sensitive only to metal lines with other counterparts, either other metal lines, or, more usually, strong hydrogen lines, and also suffer in those cases in which the velocity structure of the metal lines differs markedly from that of the counterpart line. Therefore we need a new technique to analyse the absorption structure that allows us to objectively analyse the metal data alone and to probe to the deepest possible levels that the data allow. In this paper we develop a new method that relies only on the doublet itself.

The primary metal absorption features outside of the H I forest in high-redshift quasar spectra are C IV and Si IV lines and the fact that these are doublets, and nearly all unsaturated lines, suggests an approach to this problem. In this paper we describe a pixel optical depth technique in which we analyse the spectra by looking for regions where the optical depths at the relative wavelengths of the doublet approximate the expected 2:1 ratio; we call this the superposed pixel optical depth, or “superPOD” method. We show (§3) how incompleteness of the selection arising from noise and line overlap can be quantified, and how the completeness correction can be modelled by adding artificial lines to the spectra.

The overall analysis, which parallels the methods used to generate number counts in images, allows us to probe a factor of about 0.5 dex deeper in the absorption line structure than the conventional techniques. However, even more importantly, the method is fully automatic and therefore biases and incompleteness can be handled properly. We also show (§4) how the conventional analysis can be reproduced by a percolation analysis of the optical depth results. Finally (§5) we use the data to reanalyse the evolution of the absorption with redshift, and confirm the result that there is little evolution of the distribution of the C IV absorbers over the  $z = 2 - 5$  redshift range. We assume throughout a standard  $\Lambda$ CDM cosmology with  $\Omega_m = 0.3$ ,  $\Omega_\lambda = 0.7$  and  $H_0 = 65 \text{ km s}^{-1}$ .

## 2. Observations

The quasar observations are summarized in Table 1. All of the  $z < 4$  quasars were observed with the HIRES spectrograph on the KeckI 10m telescope (Vogt et al. 1994) using the red cross disperser. Nearly all of the observations were taken prior to the replacement of the HIRES CCDs in 2004 but after the installation of the rotator, which allowed the observations to be made at the parallactic angle. A  $1.1''$  slit width was used, giving a measured resolution of 39,000. Multiple spectrograph settings were used to give complete wavelength coverage and observations spread over a number of years, from the first use of HIRES in 1994 to the present, were combined to give the final spectra. The  $z > 4$  quasars were observed with the lower resolution ESI spectrograph (Sheinis et al. 2000) on the KeckII 10m telescope. The slit width of  $0.75''$  gives a resolution of  $\sim 5300$ .

All of the reductions were carried out using an IDL software package written by the author. More details can be found in Songaila (2001; ESI) and Songaila (1998; HIRES). The individual spectra and associated noise and sky files can be found at the website <http://www.ifa.hawaii.edu/~acowie/spectra.html>. In each case we have quantified the quality of the spectrum by the signal-to-noise measured in a velocity interval of  $20 \text{ km s}^{-1}$  at two rest wavelengths (1250 and 1400 Å) in the quasar frame. The final signal-to-noise values measured in each of the spectra are shown in Table 1. The five spectra with highest quality had signal-to-noise values near or above 200 in this interval and are marked with an H in the table. We refer to this as the core quasar sample. These quasars have emission redshifts from 2.72 to 3.62.

### 3. Analysis Method

We restrict our analysis to absorption lines that lie more than  $1000 \text{ km s}^{-1}$  longward of the quasar’s Ly $\alpha$  emission and whose redshift is more than  $4000 \text{ km s}^{-1}$  blueward of the quasar redshift; this avoids contamination by the Ly $\alpha$  forest and any absorption associated with the quasar itself. The continuum was locally fit with a 7th order polynomial, iterating to remove absorption features, and the optical depth versus wavelength constructed through the chosen wavelength region for each quasar. An upper limit of  $\tau = 4.8$  was imposed where regions were saturated. The optical depth vectors were smoothed to prevent over-sampling. A  $5 \text{ km s}^{-1}$  boxcar smoothing was chosen, which roughly matches the half widths of features seen in the metal forest. A sample region of an optical depth vector can be found in Figure 1.

The distribution of optical depths in the core quasar sample is shown in Figure 2. In the selected wavelength region, 3.4% of the pixels in the optical depth vectors in the core sample have optical depths above 0.1 and about a third lie above 0.005. Much of this structure is produced by C IV, but there are contributions also from Si IV, N V and lower ionization lines as well as incompletely removed telluric features, continuum fitting errors, etc. The total optical depth can be used to provide an upper estimate of  $\Omega(\text{C IV})$ . Features with  $\tau > 0.005$  correspond to  $\Omega(\text{C IV}) < 5.8 \times 10^{-8}$  in the five quasars of the core sample. Much of this comes from higher optical depth regions;  $\tau > 0.1$  gives a contribution to this number of  $4.6 \times 10^{-8}$ . Portions of the spectrum with  $0.01 < \tau < 0.1$  give  $1.0 \times 10^{-8}$ . As we shall subsequently show, slightly more than 50% of the total absorption comes from the C IV doublets.

The doublet structure of the C IV, Si IV and N V lines can now be used to reduce the contamination by other lines or artifacts. For each wavelength position in the optical depth vector we can look at the corresponding wavelength position of the second member of the doublet and see if the optical depth is in the correct ratio of roughly 2:1. We can then restrict the optical depth vector to positions where the condition is satisfied and set the remaining positions of the vector to zero. We refer to this final vector as the cleaned optical depth. In general the measured doublet ratio will only approximate the true value because of noise, errors in the continuum fit, line contamination, etc., and we need to specify a selection parameter, that is, the range of acceptable ratios, which we refer to as the doublet ratio window. Too wide a choice of window will result in overselection of false positive signal whereas too narrow a choice will eliminate too many real systems, especially at low optical depth. We have chosen a doublet ratio window of 1:1 to 4:1 in the present work. We will discuss reasons for this choice below.

The procedure is illustrated in Figure 1. The bottom panel shows the C IV  $\lambda 1548 \text{ \AA}$  optical depth as a function of wavelength for a  $50 \text{ \AA}$  sample of spectrum, with one strong C IV

line. In the middle panel the C IV  $\lambda 1550 \text{ \AA}$  optical depth is shown in the rest frame of the C IV  $1548 \text{ \AA}$  line. Both vectors are individually smoothed as previously described. Finally, in the top panel, the result of the optical depth selection criterion of  $0.25 < \tau(1548)/\tau(1550) < 1$  is shown and confirms the strong system as a real C IV doublet while removing much of the weaker structure seen in the raw C IV  $1548 \text{ \AA}$  optical depth vector.

Figure 3 shows the procedure in a different way. Here we have plotted on the x-axis the C IV  $\lambda 1548 \text{ \AA}$  optical depth over the wavelength range, and on the y-axis the corresponding optical depth at the second member of the CIV doublet. We label these as  $\tau(1548)$  and  $\tau(1550)$  respectively. Features that correspond to uncontaminated CIV absorption will lie along the diagonal line, which is indeed seen to be heavily populated. The parallel lines show the C IV doublet ratio window, here set to  $0.25 - 1$ . Clearly a narrower window could be used at high optical depths but since there is little contamination there is no necessity for this. At lower optical depth a narrower window would result in a larger proportion of the points being scattered out of the window. In this diagram, absorption features that are not C IV fall in the lower right corner if they lie at the  $1548 \text{ \AA}$  position and in the upper left corner if they are at the  $1550 \text{ \AA}$  position. It is these features that are cleaned from the sample by the doublet ratio selection. The final cleaned optical depth is  $\tau(1548)$  for all objects that lie within the tramlines and zero for those outside.

A major advantage of this method is that it allows an objective analysis of the degree of contamination since we can compare the optical depth distribution for a true doublet — C IV, say — with a similarly generated optical depth distribution for artificial “doublets” with slightly different wavelength spacing. This is illustrated in Figure 4 where we show the plot of  $\tau(\text{artificial})$  versus  $\tau(1548)$  for an artificial doublet with a  $12 \text{ \AA}$  spacing. There are only a small number of contaminating points within the tramlines. It is also visually obvious by comparing Figure 3 ( the true doublet) with Figure 4 (the artificial doublet) that the signal of real doublets (the difference between the number of true and artificial position) persists at least to  $\tau(\text{CIV } 1548) \sim 0.01$ . The aim of the method is to find a statistical measure of the signal down to the deepest possible level.

Since the noise levels vary from spectrum to spectrum and since telluric contamination may be a function of the wavelength position, this type of analysis is best carried out individually on each quasar spectrum with the individual results subsequently being combined. Figure 5 shows the results for the  $z_{\text{em}} = 3.03$  quasar HS1946+7658, which has a S/N at the low end of the high S/N quasar core sample. The solid histogram with  $\pm 1 \sigma$  error bars in Figure 5 is the C IV  $\lambda 1548 \text{ \AA}$  optical depth distribution for lines in the spectrum selected as previously discussed. The dashed histogram is the average optical depth distribution retrieved from 20 artificial doublets with incorrect doublet separations (approximately that of

the C IV doublet) to model contamination of real C IV doublets by interloper lines, bad pixels, continuum fitting structure, telluric absorption, etc. The difference of the two histograms shown in Figure 6 is the C IV  $\lambda 1548 \text{ \AA}$  optical depth distribution statistically corrected for contamination. There is significant positive signal down to at least  $\tau(1548) \sim 0.005$ .

The distributions must also be corrected for incompleteness since lines that are contaminated by other absorption features will be missed and since noise and structure may scatter weak lines outside the selection window. That is, as well as knowing what the signal is, we also need to have an accurate estimate of the line recovery rate. We do this in standard fashion by introducing artificial lines into the real spectra and tracking the number of recoveries as a function of the C IV optical depth. The lines are added in a Monte Carlo fashion drawn from the observed core sample C IV distribution. The line widths are chosen to match the range seen in the observed absorption features but the method is not particularly sensitive to this choice. Figure 7 shows a sample strip of spectrum into which two artificial lines with  $\log N(\text{CIV}) = 11.75$  and two with  $\log N(\text{CIV}) = 12.75$  have been introduced. The panels have the same meaning as in Figure 1 and the short vertical lines in the top panel indicate the wavelengths of the introduced lines. This is the line strength at which recovery starts to break down, going from 100% at  $\log N(\text{CIV}) \sim 12$  to  $\sim 75\%$  at  $\log N(\text{CIV}) = 11.75$ . The recovery rate is also a function of the resolution of the spectra and contamination is more severe and recovery poorer in the lower resolution high-redshift ESI spectra. The final recovery rate versus optical depth is shown in Figure 8. This gives the incompleteness correction as a function of optical depth for the individual quasar spectrum, which can then be divided into the observed optical depth of Figure 6 to obtain the true optical depth distribution. For the high S/N core quasar sample, incompleteness reaches 50% at an optical depth of  $\sim 0.017$ .

#### 4. Voigt profile fitting emulation

The cleaned optical depth vector contains all the information present in the traditional cloud analyses and in general it is best to use this directly to analyse the absorption structure. However, it is interesting and very straightforward to relate the present type of analysis to the analysis by Voigt profile fitting and to see how well we reproduce the results previously obtained by this method. In addition, we can use the method to characterize the local environment in which a given optical depth point lies.

We can use the superPOD method to emulate the usual Voigt profile fitting analysis of the spectra in an objective way. The basis of this is to generate ‘pseudo-cloud complexes’ by combining neighboring optical depths with detections into a single line profile. We do this by first finding the maximum optical depth in the true optical depth vector. We then

define the cloud complex as all positions with non-zero optical depths that are connected to the primary position, with gaps where the optical depth is zero being less than  $100 \text{ km s}^{-1}$ . An example of a complex picked out in this way is shown in Figure 9. Positions already allocated to cloud complexes are eliminated from the cleaned optical depth vector and the process repeated. The column density is computed for each cloud complex from the integral of the optical depths included in it, with each optical depth being weighted by the completeness and contamination correction for that optical depth.

The exact definition of ‘neighboring’ is somewhat arbitrary in the use of the  $100 \text{ km s}^{-1}$  window to define the cloud size. In general, the wider the ‘cloud’ window, the more likely one is to lose lower column density clouds as individual entities: they would be incorporated into broader ‘cloud complexes’. However, in practice, for reasonable values of the window the results are not too sensitive to this choice. We illustrate this in Figure 10, where we show the number of clouds found as a function of column density for velocity windows of  $75 - 300 \text{ km s}^{-1}$ . The wider window reduces the number of independent low column density complexes but the effect is not large.

In Figure 11 we show as open squares the raw C IV column density distribution of pseudo-clouds obtained from C IV optical depths retrieved by the superPOD method from the core quasar sample at an average redshift of 2.7. The filled squares with  $1 \sigma$  error bars show the distribution corrected for incompleteness and bias. For comparison, the open circles show the results of a traditional analysis of the same set of objects, conducted in the usual way with visual identification of lines and subsequent manual Voigt profile fitting. The best-fit line has a slope of  $-1.44$ , similar to the result of Ellison et al. (2000) at the same redshift. This is the dashed line in Figure 11. The solid line has a slope of  $-1.7$ , based on fitting only to complexes with  $N > 10^{13} \text{ cm}^{-2}$ .

Using the various quasar samples of Table 1 at low and high redshifts, we have constructed in this way the C IV column density distributions in the redshift range  $1.5 - 5.5$ . In general, the superPOD method using pseudo-cloud generation reproduces the invariance of C IV column density distribution function with redshift already determined by traditional methods (Songaila 1997, 2001; Pettini et al. 2003) and, with an extra sensitivity of about 0.5 dex over these previous results, the redshift invariance of the distribution functions is seen very clearly. Following the methods used in the previous studies, we can also construct  $\Omega(\text{CIV})$  as a function of redshift, and this is shown in Figure 12. This agrees very well with the traditional studies in showing that  $\Omega(\text{CIV})$  remains nearly invariant between redshifts 2 and 5. This remains true whether counting stronger absorbers (open squares:  $13 < \log N(\text{CIV}) < 14$ ) or all absorbers (filled squares:  $12 < \log N(\text{CIV}) < 15$ ).



We can extend the method by computing the column densities of lines corresponding to other species for the range of velocities in each C IV - selected cloud complex. For doublets such as Si IV we use the cleaned optical depth for that species while for singlets such as C II we simply use the raw optical depth. These ion ratios are shown as a function of redshift for the stronger cloud complexes in Figures 13 and 14. In both figures, the small filled squares denote the ion ratios determined from the C IV pseudo-clouds (with width of  $100 \text{ km s}^{-1}$ ), whereas the open diamonds show the median ion ratios in each redshift bin determined directly from the optical depths. Figure 13 demonstrates that neither the range nor the median value of C II/C IV changes significantly as a function of redshift, agreeing with Schaye et al.(2003). However, the same is not true of Si IV/C IV, a result which a Kolmogorov-Smirnov test (Figure 15) shows to be highly significant. The large open squares in Figure 14 denote pseudo-clouds with high C IV column density. The K-S test is based on all the Si IV and C IV systems, including these strong ones. However, it is dominated by the larger numbers of smaller column density systems. On the other hand, evolution in both  $\Omega(\text{CIV})$  and  $\Omega(\text{SiIV})$  is dominated by the high column density end of the distribution. We discuss this further, using optical depth vectors, in Paper II, and we postpone the interpretation to that paper.

In Figure 16 we show the distribution of the optical depths as a function of the column density of the cloud complex in which they lie. For the HIRES data there is a tight relation ( $\tau \sim N^{0.7}$ ) between the peak optical depth and the column density, which is washed out in the lower resolution ESI data. In paper II we shall revisit this relation, which implies that higher column density clouds, or, equivalently, systems with larger peak optical depths, are also wider in velocity space.

## 5. Optical depth analysis

It is encouraging that there is such good agreement between traditional Voigt profile fitting methods and the objective, but still slightly arbitrary, method of generating pseudo-cloud complexes. However, the real merit of the superPOD technique lies in the fact that the cleaned optical depth vectors contain all of the information about the amount of material, its distribution in strength, and the velocity structure of the absorption, and may be used directly to characterize these without ever resorting to arbitrary groupings.

In the present paper we use the optical depth vectors to determine the metallicity evolution directly from C IV and Si IV optical depths, postponing a discussion of the velocity structure and the ionization balance evolution to Paper II. Our results are shown in Figure 17 for C IV (filled squares) and Si IV (filled diamonds) in four redshift bins, [1.5,2.5], [2.5,3.5],

[3.5,4.5], and [4.5,5.5]. We see about a factor of two turndown in C IV at  $z = 5$  and perhaps a larger turndown in Si IV at the same redshift. The S/N of the data is declining at the highest redshifts and the sky systematics are higher but, even given these caveats, the slight turndown at these redshifts seems real and could correspond to a decline in the metal density or a change in the ionization balance (Shaye et al. 2003). Irrespective of this point there is clearly a significant metal density in place at  $z = 5$ .

In Figure 18 we show the optical depth distributions of C IV over the same redshift ranges. We have divided the quasar sample into five sets of five quasars, ordered by redshift, which are shown in the five panels, (a) to (e). (We omitted the quasar PSS0747+443 and divided the remainder to give the five groups.) The redshift range of C IV absorption in each set of quasars is marked on the panel. The three highest redshift panels are based on ESI data and the two lowest on HIRES data. In each case we have overplotted the distribution obtained from the core high S/N quasar sample. For the ESI data we have smoothed the comparison sample to the ESI resolution. Rather than show Poisson error bars, which underestimate the errors because of correlation effects, we have shown in each case the range of the five quasars. There is very little change in the shape of the distribution over the redshift interval, which is consistent with the results of the Voigt profile analyses.

The slow change in the overall ion densities and the invariance of the distribution functions appear to suggest that contemporary injection must not be a dominant mechanism for producing the observed absorption lines, since we would in that case expect the features to track the evolution of the star-forming galaxies and to have some dependence on the changing properties of these objects. Indeed, even if this were the only mechanism present, we would expect that metals ejected by previous generations of star-forming galaxies would build up in the intergalactic gas, and that as time progressed the relative numbers of these versus those being formed by contemporary injection would change, so producing evolution in the column density distribution with redshift. However, such effects could be concealed if the ejected material becomes too hot to be observed as C IV (Aguirre et al. 2004), and in the second paper of this series we will look at other approaches to determining the fraction of the lines that arise in contemporary injection.

## 6. Conclusion

We have described a novel objective pixel optical depth technique, “superPOD”, that uses the doublet nature of the common ions C IV and Si IV, that are the principal metal tracers in the intergalactic medium outside of the Ly $\alpha$  forest, to analyze the properties of metals in the high redshift intergalactic medium using a sample of extremely high signal-to-

noise Keck HIRES and ESI spectra of 26 quasars between redshifts 2.1 and 6.4. The method is completely objective and, using statistical corrections for contamination by other lines, telluric absorption, bad pixels, continuum fitting, etc. and for incompleteness, gives us an increased sensitivity of approximately 0.5 dex over previous analyses.

As a check on the method, we have reproduced the conventional analysis using a percolation method to generate pseudo-clouds from ion optical depths. Using this set of pseudo-clouds we confirm that the C IV column density distribution remains essentially invariant, with slope  $-1.44$ , from  $z = 1.5$  to  $z = 5$ , which confirms the lack of redshift evolution of  $\Omega(\text{CIV})$  for  $z = 2$  to  $z = 5$  previously determined from conventional Voigt profile fitting analysis.

The pseudo-clouds also give information on the column density environment of a given optical depth: for the higher resolution HIRES data there is a tight relation,  $\tau \sim N^{0.7}$ , between the peak optical depth and the column density.

Using the optical depths directly, we show that there is little evolution in C IV and C II/C IV from  $z = 2$  to  $z = 5$ , though there is a turndown of at least a factor of two in  $\Omega(\text{CIV})$  and  $\Omega(\text{SiIV})$  above  $z = 5$ ; we do, however, see substantial evolution in Si IV/C IV.

We will use this technique in two subsequent papers to investigate what fraction of the absorbers lie in galactic wind outflows (Paper II) and what metallicity is associated with regions of  $\tau(\text{Ly}\alpha) < 1$  (Paper III).

I would like to thank X. Fan and R. Becker for providing the coordinates of some of the  $z > 6$  quasars prior to their publication. This research was supported by the National Science Foundation under grant AST 00-98480.

## REFERENCES

- Adelberger, K. L., Steidel, C. C., Shapley, A., & Pettini, M. 2003, ApJ, 584, 45.
- Aguirre, A., Schaye, J. & Theuns, T. 2002, ApJ, 576, 1
- Aguirre, A., Schaye, J., Kim, T.-S., Theuns, T., Rauch, M. & Sargent, W. L. W. 2004, ApJ, 602, 38
- Aguirre, A., Schaye, J., Hernquist, L., Kay, S., Springel, V. & Theuns, T. 2005, ApJ, 620, L13
- Aracil, B., Petitjean, P., Pichon, C., & Bergeron, J., 2004, AA, 419, 811.

- Bromm, V., Yoshida, N., & Hernquist, L. 2003, *ApJL*, 596, L135
- Cowie, L. L., Songaila, A., Kim, T.-S., & Hu, E. M. 1995, *AJ*, 109, 1522
- Cowie, L. L. & Songaila, A. 1998, *Nature*, 394, 44
- Daigne, F., Olive, K. A., Vangioni-Flam, E., Silk, J., & Audouze, J. 2004, *ApJ*, 617, 693
- D’Odorico, S., Cristiani, S., Dekker, H., Hill, V., Kaufer, A., Kim, T.-S., Primas, F. 2000, *SPIE* 4005, 121
- Ellison, S. L., Songaila, A., Schaye, J. & Pettini, M. 2000, *AJ*, 120, 1175
- Fujita, A., Mac Low, M.-M., Ferrara, A., & Meiksin, A. 2004, *ApJ*, 613, 159
- Mackey, J., Bromm, V., & Hernquist, L. 2003, *ApJ*, 586, 1
- Madau, P., Ferrara, A., & Rees, M. J. 2001, *ApJ*, 555, 92.
- Meyer, D. M., & York, D. G. 1987, *ApJL*, 315, L5
- Pettini, M., Steidel, C. C., Adelberger, K. L., Dickinson, M., & Giavalisco, M. 2000, *ApJ*, 528, 96
- Pettini, M., Madau, P., Bolte, M., Prochaska, J. X., Ellison, S. L., & Fan, X. 2003, *ApJ*, 594, 695
- Pichon, C., Scannapieco, E., Aracil, B. et al. 2003, *ApJ*, 597, L97.
- Qian, Y.-Z., Sargent, W. L. W., & Wasserburg, G. J. 2002, *ApJL*, 569, L61
- Schaye, J., Aguirre, A., Kim, T.-S., Theuns, T., Rauch, M. & Sargent, W. L. W. 2003, *ApJ*, 596, 768
- Simcoe, R. A., Sargent, W. L. W., & Rauch, M. 2004, *ApJ*, 606,92
- Songaila, A. 1997, *ApJL*, 490, L1
- Songaila, A. 1998, *AJ*, 115, 2184
- Songaila, A. 2001, *ApJ*, 561, L153
- Songaila, A. & Cowie, L. L. 1996, *AJ*, 112, 335
- Tytler, D., et al. 1995, in *QSO Absorption Lines*, ESO Astrophysics Symposia, ed. G. Meylan (springer, Heidelberg), p. 289
- Venkatesan, A., & Truran, J. 2003, *ApJL*, 594, L1
- Vogt, S. S. et al. 1994, *SPIE*, 2198, 362
- Wasserburg, G. J., & Qian, Y.-Z. 2000, *ApJL*, 538, L99

Yoshida, N., Bromm, V., & Hernquist, L. 2004, *ApJ*, 605, 579.

Table 1. The Quasar Sample

Quasar	$z_{em}$	S/N 1250 Å	S/N 1400 Å	Instr. <sup>(a)</sup>	Sample <sup>(b)</sup>
SDSS1148+52	6.39000	80	-5	E	?
SDSS1048+46	6.23000	75	-5	E	?
SDSS1306+03	5.98500	95	-5	E	4
SDSS0836+00	5.76500	130	55	E	4
SDSS1044-01	5.75500	70	25	E	4
SDSS1204-00	5.05500	105	80	E	4
SDSS0338+00	4.99000	115	45	E	4
SDSS1737+58	4.84000	100	115	E	3,4
SDSS2200+00	4.76300	125	65	E	3,4
BR1202-0725	4.60000	135	95	E	3
BR0334-1612	4.36000	130	85	E	3
BR0353-3820	4.55500	100	60	E	3
BR2237-0607	4.55000	230	220	E	3
PSS0747+443	4.43200	95	60	E	3
BRI0952-011	4.40800	100	90	E	3
PSS0926+305	4.19000	135	120	E	3
BR2237-0607	4.55000	55	35	HH	?
Q1422+2309	3.62000	340	285	H	H,2
HS0741+4741	3.22000	210	185	H	H,2
Q0636+680	3.18000	220	165	H	H,2
HS1946+7658	3.03000	210	200	H,HH	H,2
HE2347-4342	2.88000	115	105	H	1
HS0119+1432	2.87000	115	95	H	1
HS1700+6416	2.72000	205	175	H	H,1
HE1122-1648	2.40000	60	75	H	1
HS1626+6433	2.31000	55	80	H	1

Table 1—Continued

Quasar	$z_{em}$	S/N 1250 Å	S/N 1400 Å	Instr. <sup>(a)</sup>	Sample <sup>(b)</sup>
Q1331+170	2.08000	30	110	H	1

<sup>(a)</sup>E : ESI spectrograph on the Keck II telescope; H : Hires spectrograph on the Keck I telescope; HH : HIRES with upgraded detector

<sup>(b)</sup>H : high S/N sample; 1,2,3,4 : samples with  $\langle z \rangle = 2.2, 2.8, 3.9, 4.5$

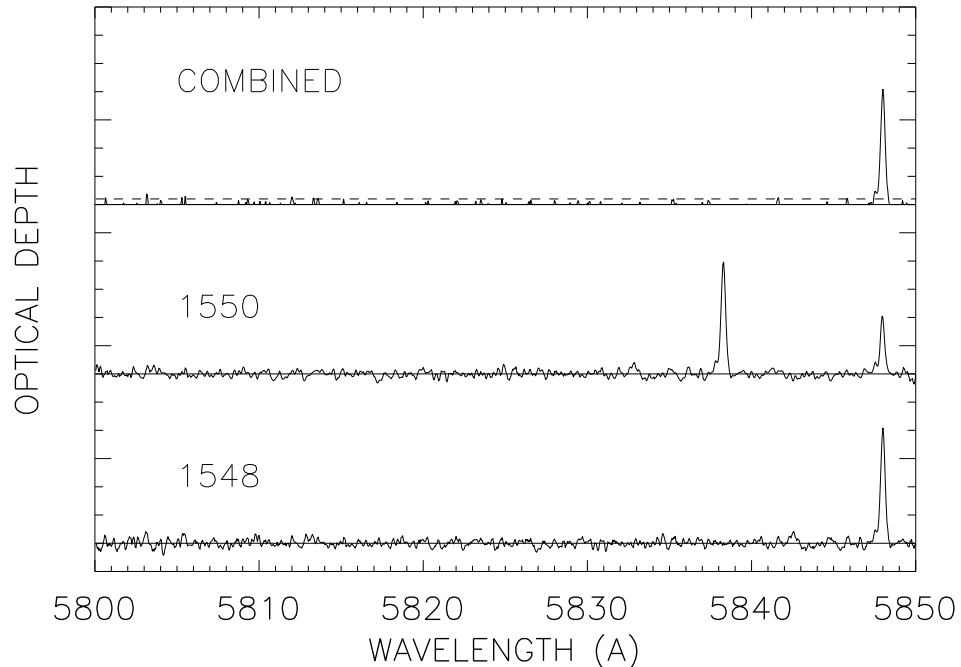


Fig. 1.— Illustration of the doublet selection method based on a portion of the spectrum of the quasar HS1946+7658. *Bottom panel:* C IV  $\lambda 1548$  Å optical depth as a function of wavelength for a 50 Å sample of spectrum, with one strong C IV detection. *Middle panel:* corresponding C IV  $\lambda 1550$  Å optical depth shifted to the  $\lambda 1548$  frame. *Top panel:* result of the optical depth selection criterion of  $0.25 < \tau(1548)/\tau(1550) < 1$ , confirming the system as a real C IV doublet. The optical depth distributions have been smoothed to  $5 \text{ km s}^{-1}$ , to roughly Nyquist sample the typical CIV line widths in these spectra. Only a small number of points in the noise satisfy the doublet ratio window and appear as noise spikes in the cleaned vector of the upper panel. Below a wavelength of 5840 Å in the lower panel approximately 20% of the 409 independent pixels have a raw  $\tau(1548)$  above 0.005. Just over three quarters of these are eliminated by the doublet ratio filter, leaving 19 pixels in the cleaned  $\tau(1548)$  vector of the upper panel which have values above 0.005. (The dashed line in the top panel indicates an optical depth of 0.01 to show the scale on the figure. It is not a cutoff level.)



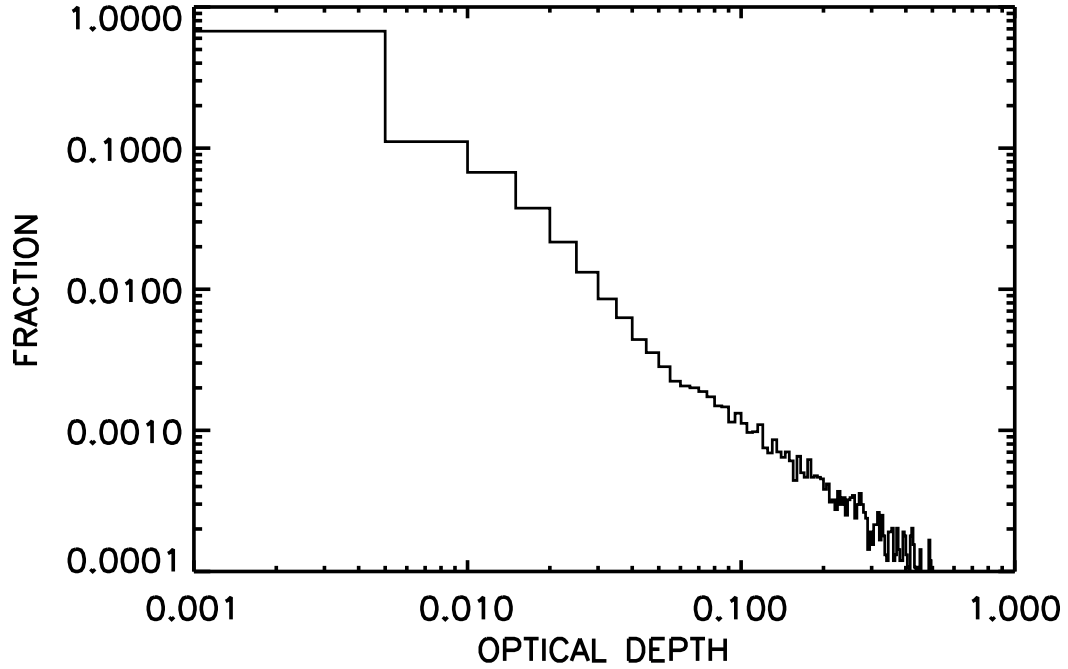


Fig. 2.— Distribution of optical depths over the C IV wavelength region in the core quasar sample. The result is shown as the fraction of the total number of pixels lying in 0.005 wide bins in the optical depth. Only 3.4% of the pixels have optical depths above 0.1. Roughly one third of the pixels have optical depths above 0.005.

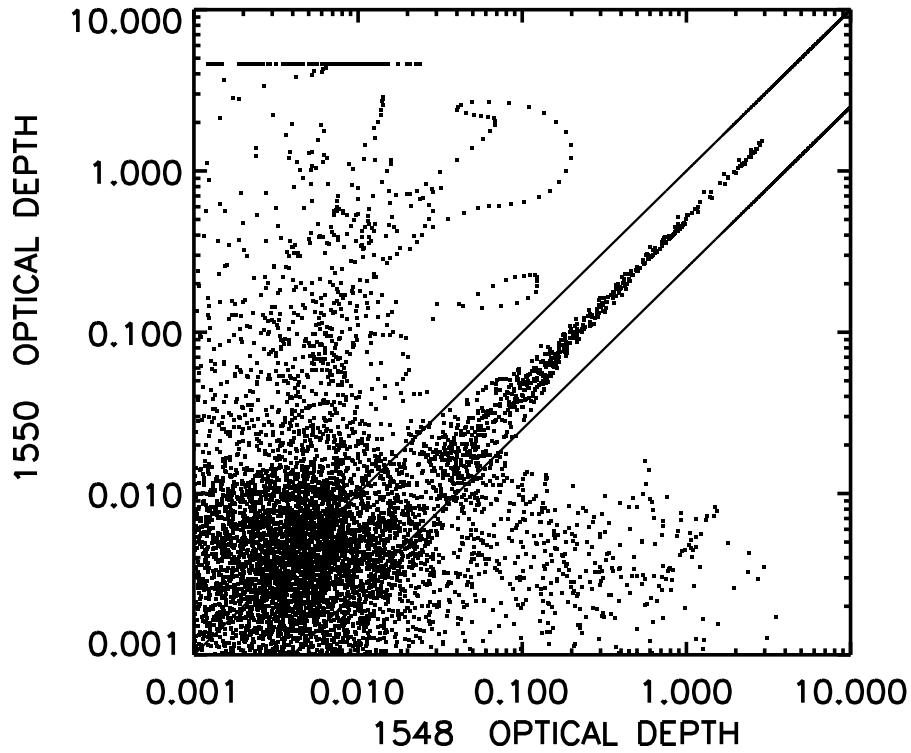


Fig. 3.—  $\lambda 1550 \text{ \AA}$  optical depth vs  $\lambda 1548 \text{ \AA}$  optical depth for all the measured optical depths in HS1946+7658. *Solid lines*: optical depth selection criteria of  $0.25 < \tau(1548)/\tau(1550) < 1$ . Detected C IV doublets are clearly present visually down to  $\tau(1548) \sim 0.01$ . Only positions with  $\tau(1548) < 4$  are plotted. Saturated regions appear at  $\tau = 4.8$  in the  $\tau(1550)$  axis.

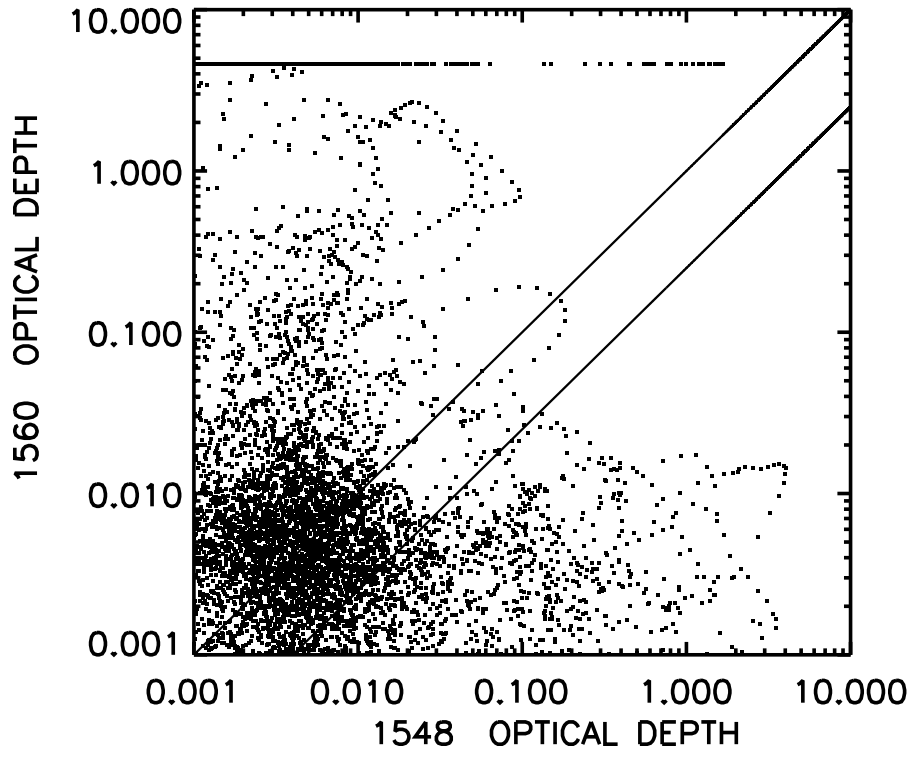


Fig. 4.— As in Fig. 2 for artificially generated 'false doublets' with doublet separation of 12 Å. The solid lines have the same meaning as in Figure 3.

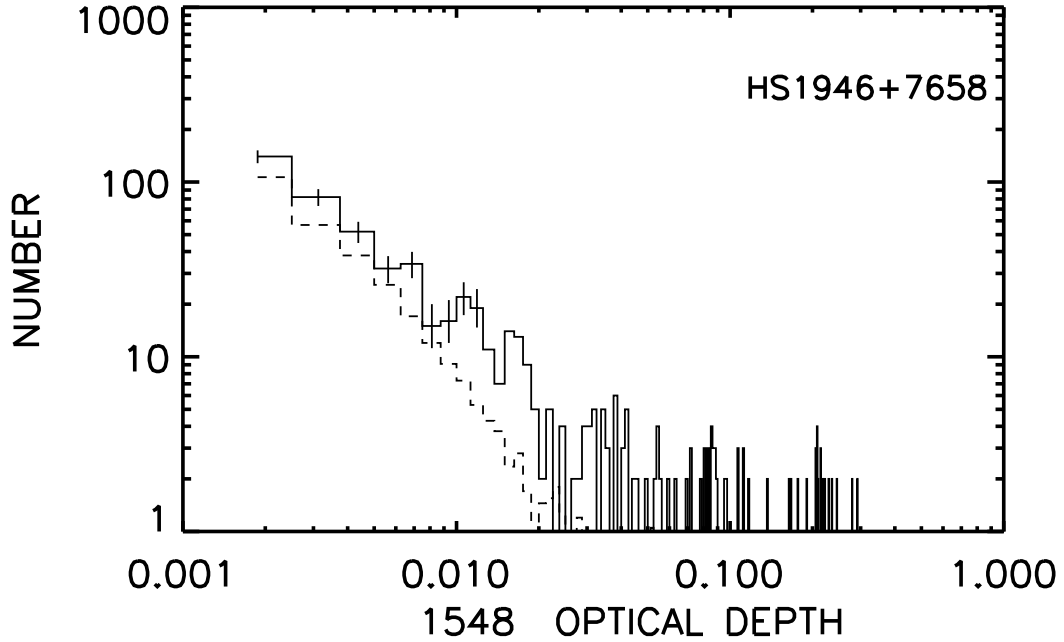


Fig. 5.— *Solid histogram*: C IV  $\lambda 1548 \text{ \AA}$  optical depth distribution for selected lines in the spectrum of the  $z_{\text{em}} = 3.03$  quasar HS 1946+7658. Error bars are  $\pm 1 \sigma$ . Lines were chosen as illustrated in Figs. 1 and 2. *Dashed histogram*: average optical depth distribution retrieved from 20 artificial doublets with incorrect doublet separations to model contamination of real C IV doublets by interloper lines, bad pixels, telluric absorption, etc.

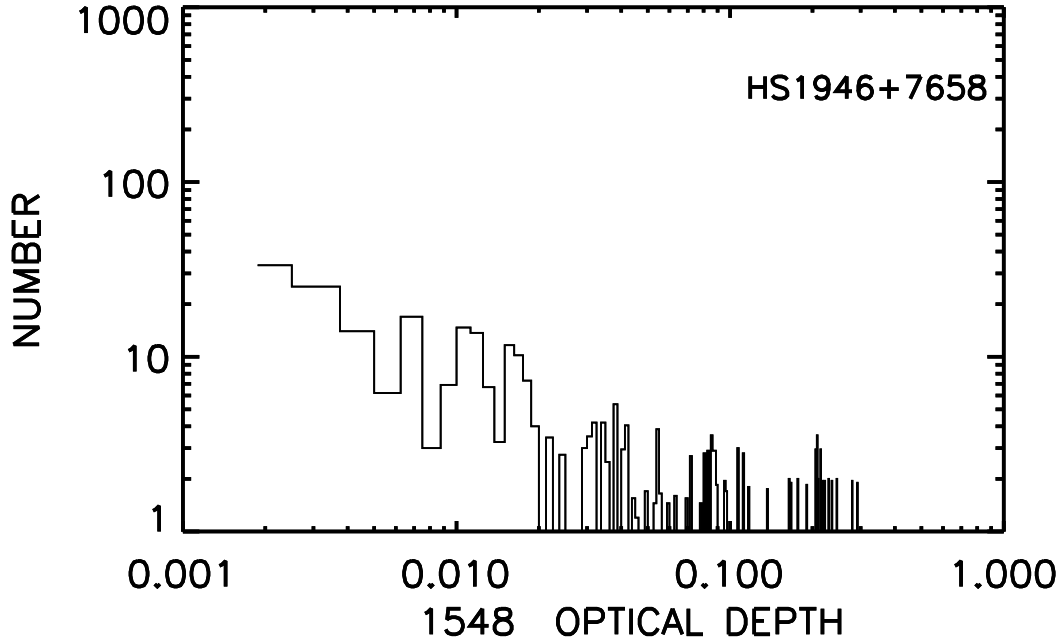


Fig. 6.— Difference between the solid and dashed histograms of Figure 5, illustrating the C IV  $\lambda 1548$  Å optical depth distribution statistically corrected for contamination. There is significant positive signal down to  $\tau(1548) \approx 0.005$ .

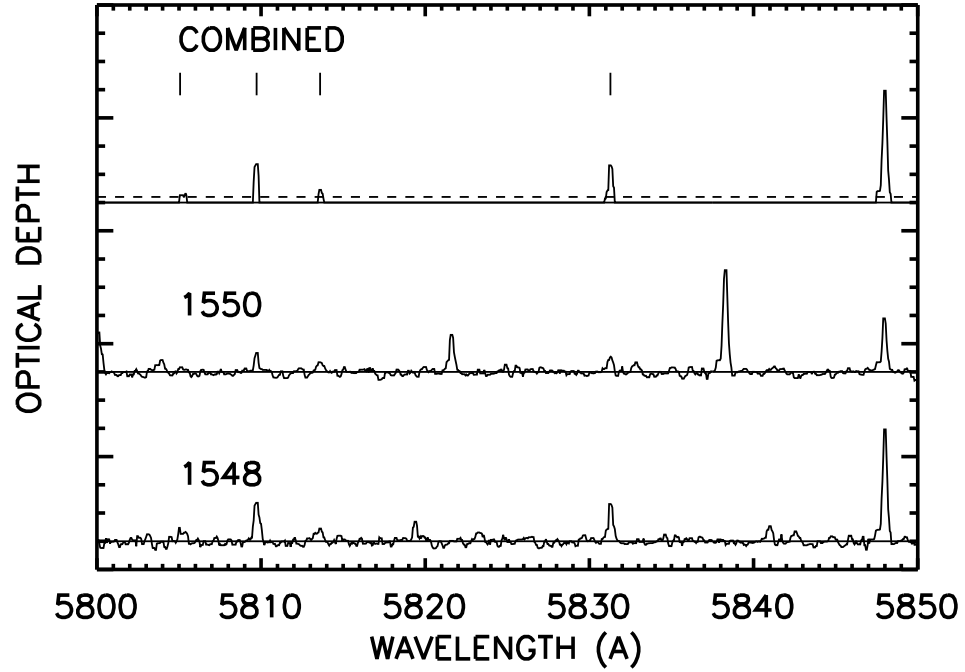


Fig. 7.— Illustration of the method of measuring the recovery rate of artificial doublets. Two artificial C IV doublets with column density  $\log N(\text{C IV}) = 11.75$  and two with  $\log N(\text{C IV}) = 12.75$  have been inserted into the region of the spectrum of HS1946+7658 shown in Figure 1. The panels have the same meaning as in Fig. 1. Short vertical lines in the top panel show the wavelengths of the introduced artificial lines.

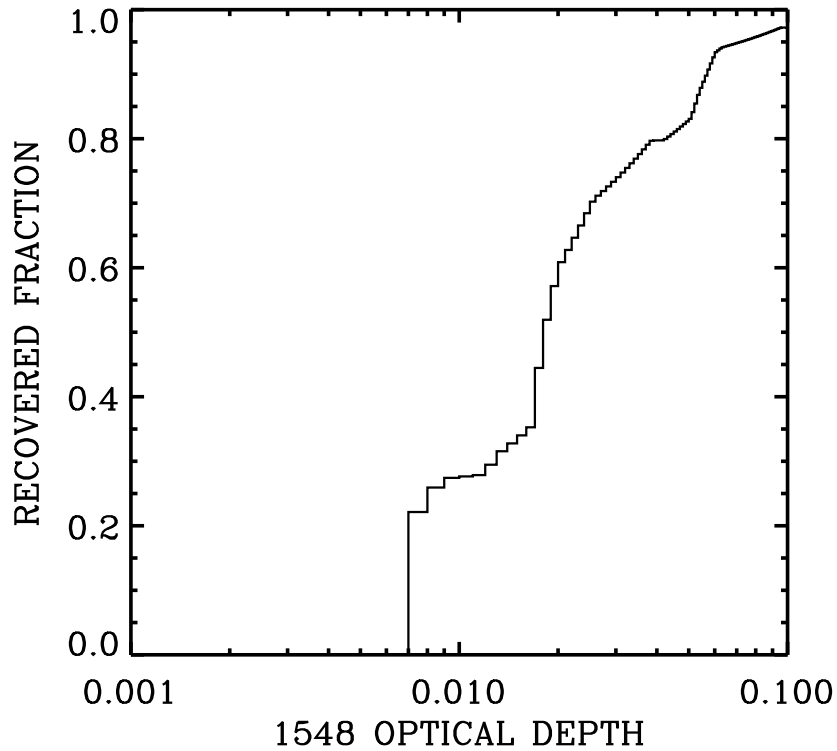


Fig. 8.— Fraction of recovered pixels as a function of the input optical depth in the 1548 Å line for the 5 quasars in the core quasar sample. At higher optical depths the small incompleteness is primarily caused by line blending. The recovery begins to drop rapidly at lower optical depths because of noise scattering which moves ratios outside the doublet window. The recovery in these quasars drops to 0.5 at  $\tau = 0.017$  and to 0.25 at  $\tau = 0.007$ , at which point we consider we have reached the useful limit of the data.

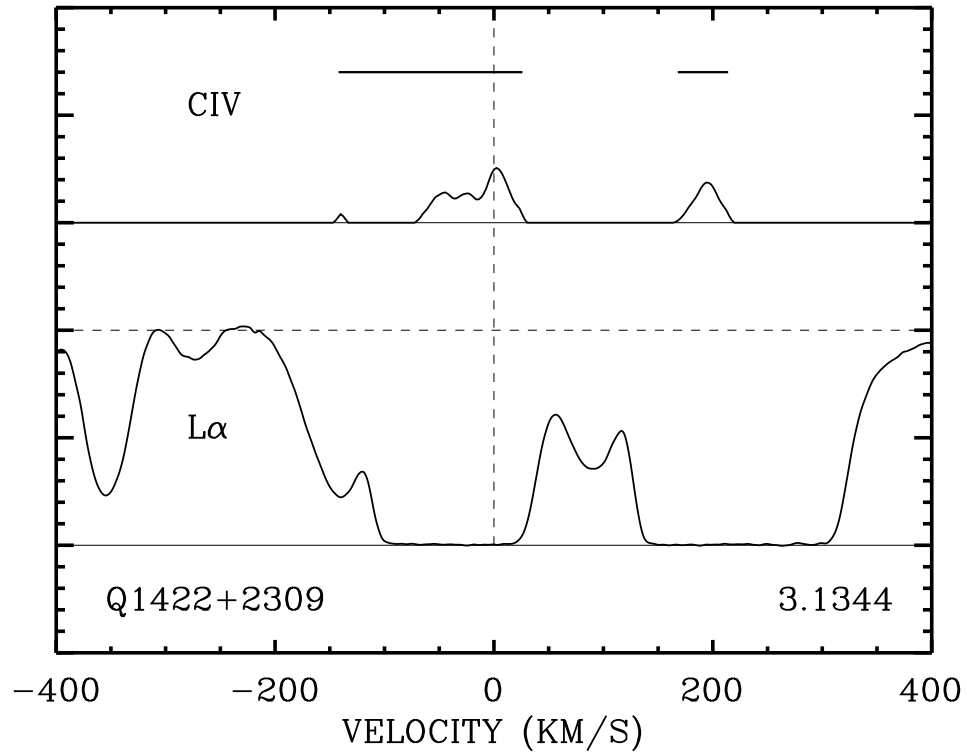


Fig. 9.— Illustration of the generation of cloud complexes in a region of the spectrum of the quasar Q1422+2309. *Top panel:* cleaned C IV optical depth vector. The analysis, with a  $100 \text{ km s}^{-1}$  cloud window, splits this region into two complexes that are marked by the horizontal solid lines. *Lower panel:* corresponding region of the Ly $\alpha$  line, which shows that the complex breakdown matches well to the Ly $\alpha$  structure. However, the exact breakdown is subject to the exact choice of window. A  $150 \text{ km s}^{-1}$  window would reduce this particular system to one complex whereas a  $50 \text{ km s}^{-1}$  window would split it into three parts.



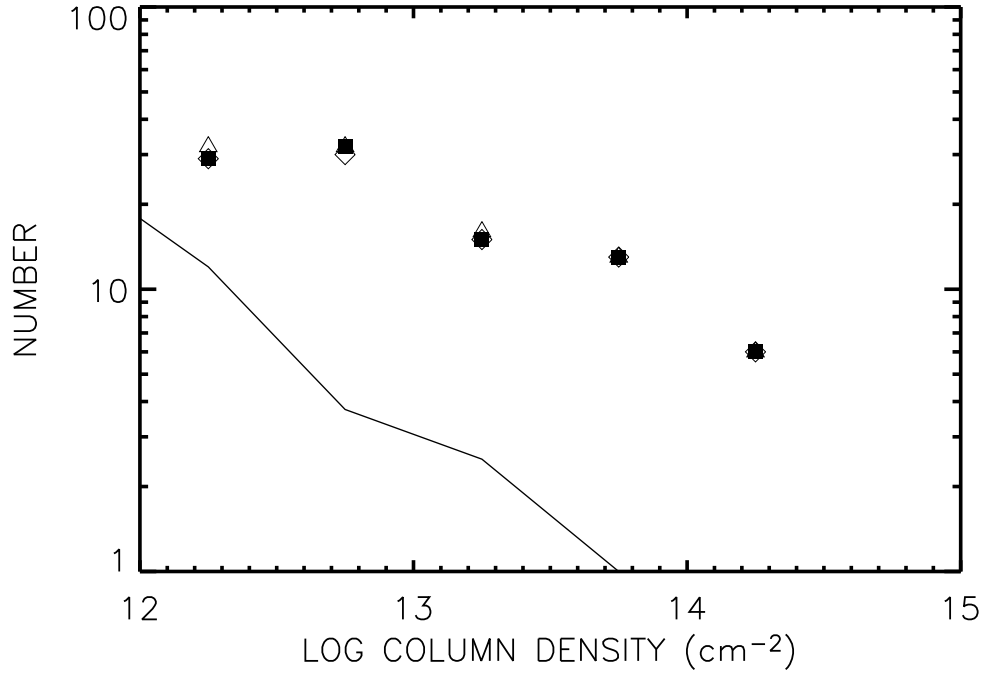


Fig. 10.— Number of complexes retrieved in the core quasar sample as a function of column density for three velocity windows:  $75 \text{ km s}^{-1}$  (*triangles*),  $150 \text{ km s}^{-1}$  (*squares*), and  $300 \text{ km s}^{-1}$  (*diamonds*). The effect of widening the window is to blend weaker systems into larger complexes and so reduce the number of low column density systems but, as can be seen from the figure, the effect is not large for reasonable values of the velocity window. *Solid line*: number of systems found as a function of column density for a set of artificial doublets approximating the C IV separation; this shows the degree of contamination at a given column density.

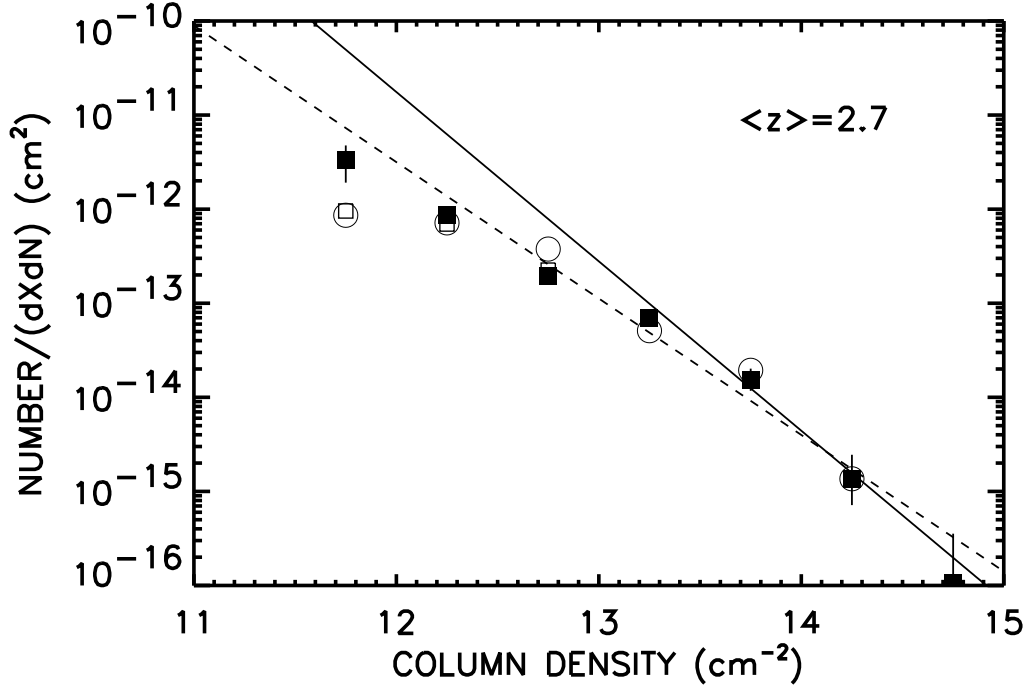


Fig. 11.— *Open squares*: C IV column density distribution of pseudo-clouds determined using a velocity window of  $100 \text{ km s}^{-1}$  (see text) from the C IV optical depths retrieved by the superPOD method from the core quasar sample. The average C IV redshift is 2.7. *Filled squares*: distribution corrected for incompleteness, with  $1 \sigma$  error bars. *Open circles*: distribution obtained by Voigt profile fitting of C IV doublets selected by hand from the spectra, with no incompleteness correction. *Dotted line*: fit to the data with power law index  $-1.44$ . *Solid line*: power law slope  $= -1.7$ , which fits the  $N(\text{C IV}) > 10^{13} \text{ cm}^{-2}$  sample.

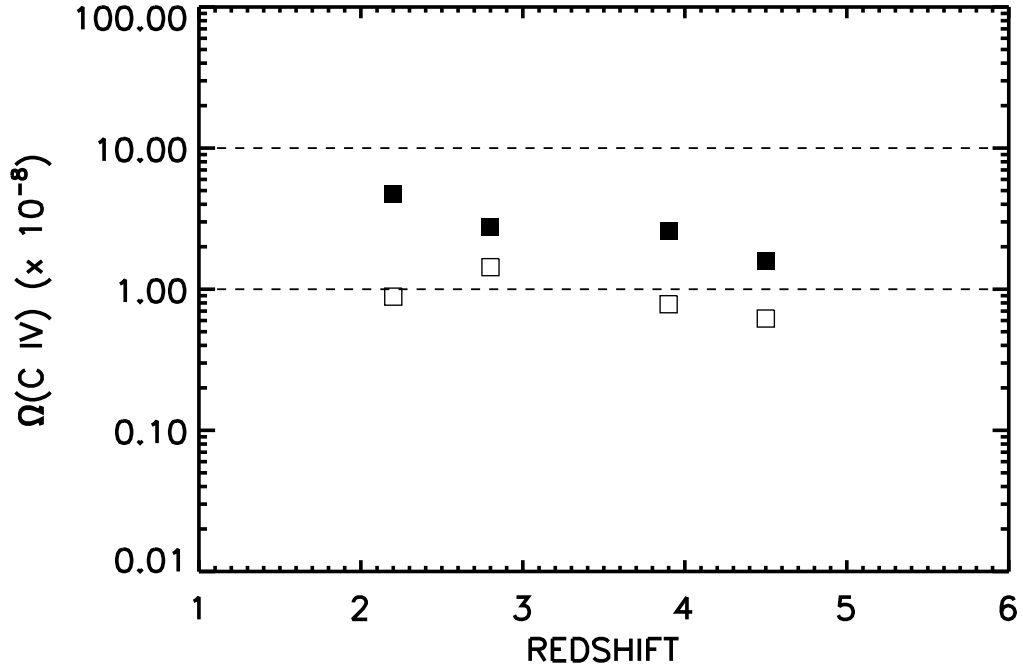


Fig. 12.— *Filled squares*:  $\Omega(\text{CIV})$  as a function of redshift computed from C IV column density distributions of pseudo-clouds with  $12 < \log N(\text{CIV}) < 15$  obtained from C IV optical depths retrieved by the superPOD method from various samples of quasars with  $2 < z < 5.5$ . *Open squares*: as above, with  $13 < \log N(\text{CIV}) < 14$ .

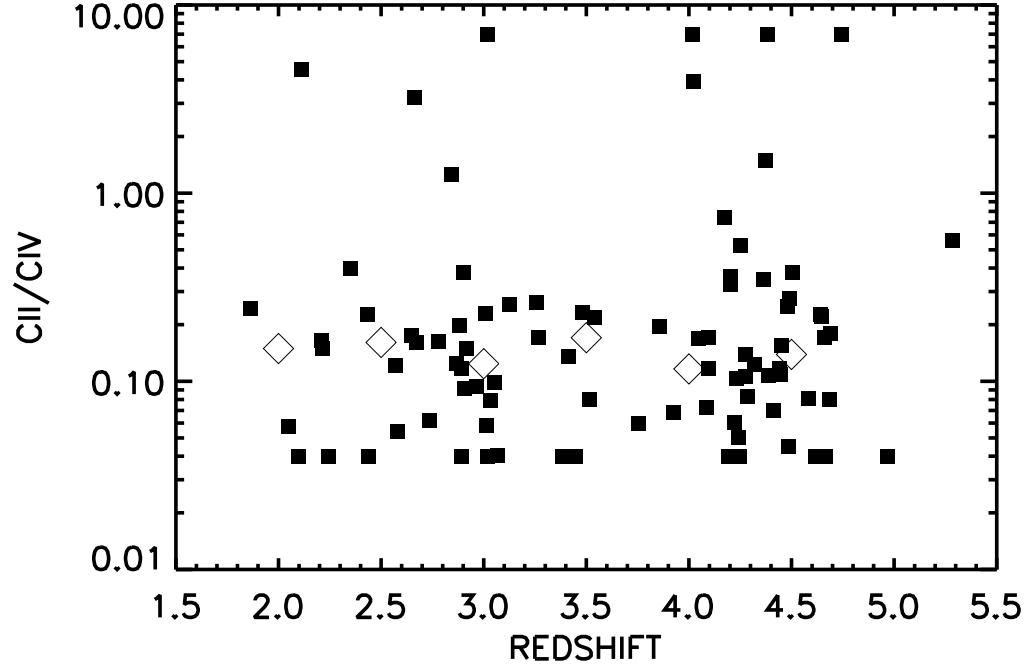


Fig. 13.— *Small filled squares*: C II/C IV as a function of redshift determined from the integrated strengths of C II and C IV in C IV-selected pseudo-clouds (see text) with a width of  $100 \text{ km s}^{-1}$ . C II optical depth vectors have not been cleaned to remove contamination. *Large open diamonds*: median value of C II/C IV in each redshift bin, calculated directly from C II and C IV optical depth vectors.

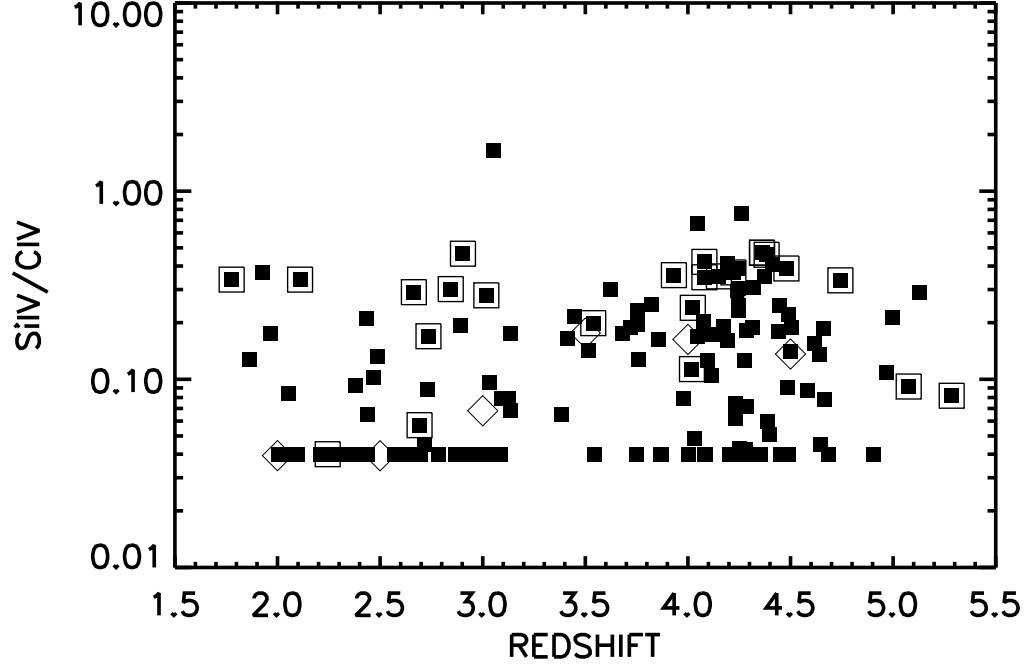


Fig. 14.— *Small filled squares*: Si IV/C IV as a function of redshift determined from the integrated strengths of Si IV and C IV in C IV-selected pseudo-clouds (see text) with a width of  $100 \text{ km s}^{-1}$ . Both Si IV and C IV optical depths have been cleaned to remove contamination (see text). *Large open diamonds*: median value of Si IV/C IV in each redshift bin, calculated directly from Si IV and C IV optical depth vectors. *Large open squares*: positions of strong absorbers with  $N(\text{C IV})$  and  $N(\text{C II}) > 10^{14} \text{ cm}^{-2}$ .

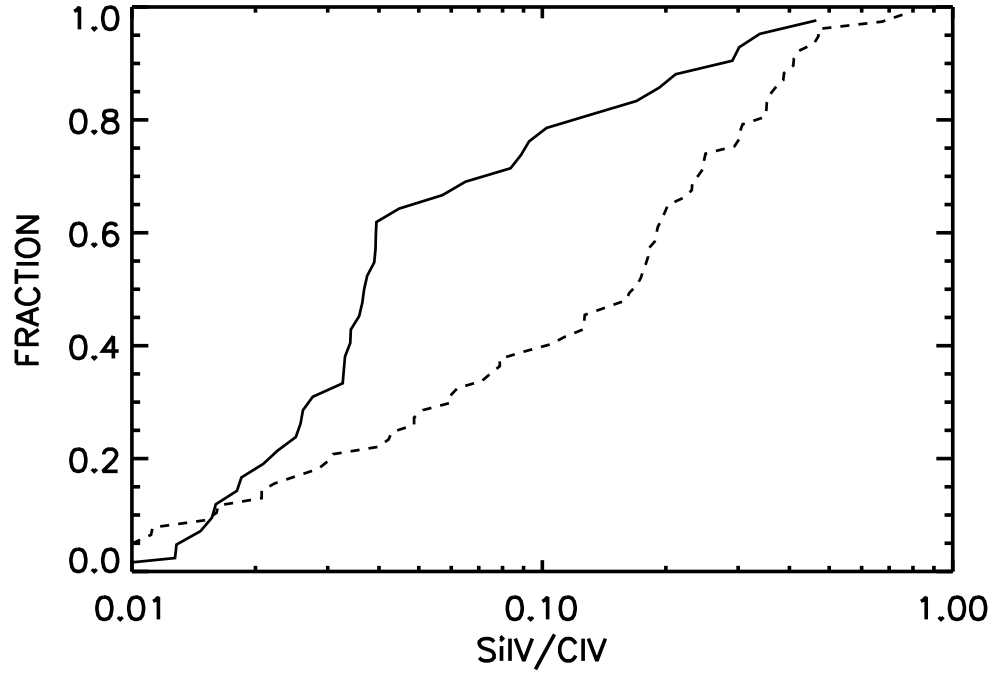


Fig. 15.— Kolmogorov-Smirnov test of the hypothesis that the Si IV/C IV ratio in the cloud complexes at  $3.5 < z < 4.5$  (*dashed line*) is the same as at  $2 < z < 3$  (*solid line*). The Si IV/C IV ratios are significantly weighted to higher values at the the higher redshifts despite the fact that the distribution of C IV column densities has not changed.

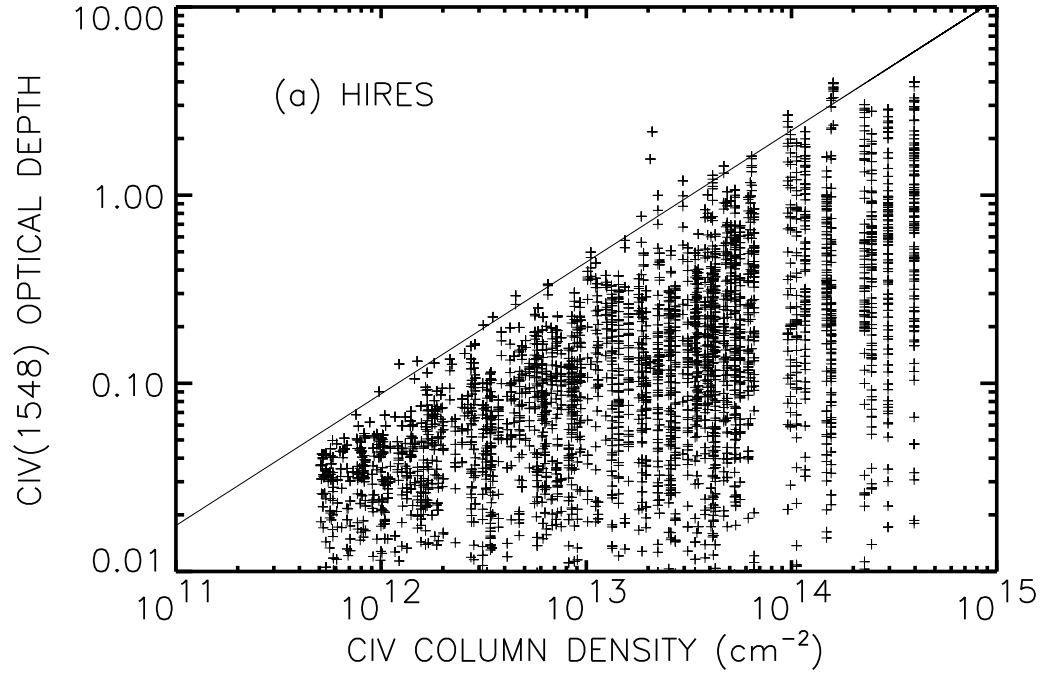


Fig. 16a.— Cleaned C IV(1548) optical depths versus the column density of the complex in which they lie. HIRES data are shown in panel (a) and ESI data in panel (b). For the HIRES data, there is a tight relation,  $\tau \sim N^{0.7}$  (*solid line*) between the peak optical depth and the column density of the complex. This is washed out in the lower resolution ESI data.

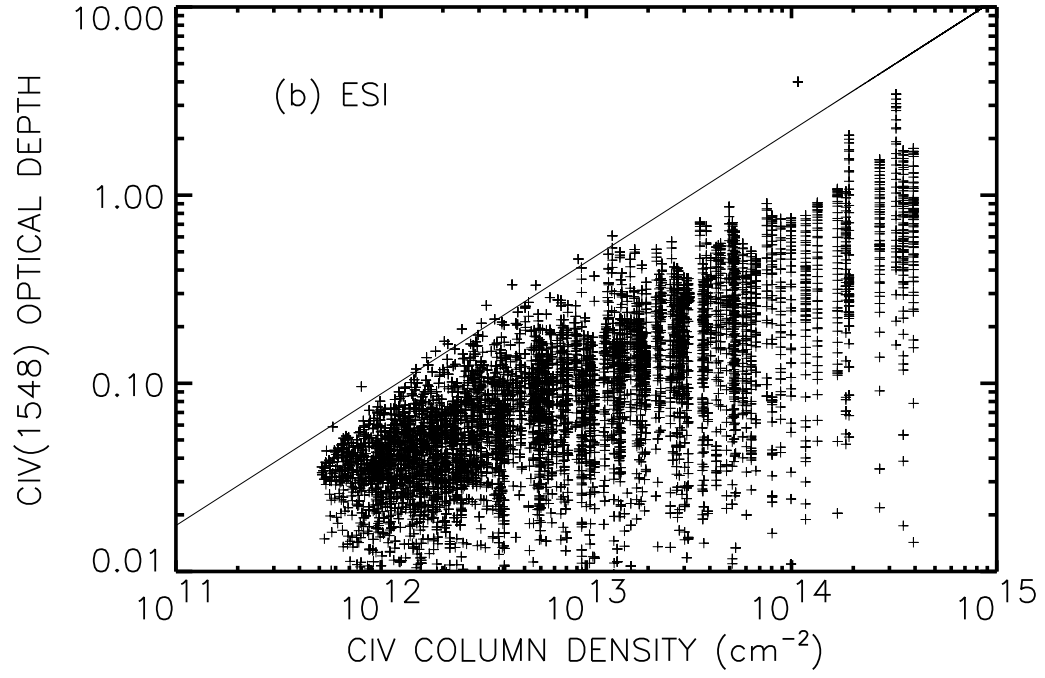


Fig. 16b.—



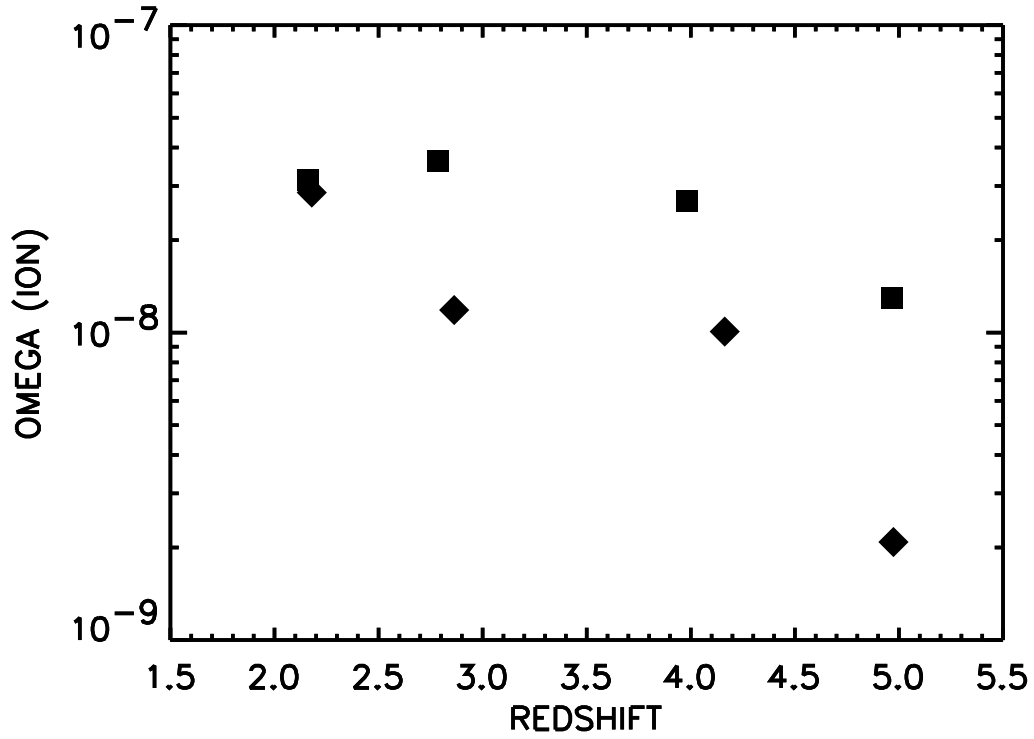


Fig. 17.— *Filled squares*: average  $\Omega(\text{CIV})$  as a function of redshift computed directly from C IV optical depths retrieved by the superPOD method from various samples of quasars with  $2 < z < 5.5$ . Redshift bins are  $[1.5, 2.5]$ ,  $[2.5, 3.5]$ ,  $[3.5, 4.5]$ ,  $[4.5, 5.5]$ , with the observation shown at the mean redshift in the interval. *Filled diamonds*: as above, for Si IV.

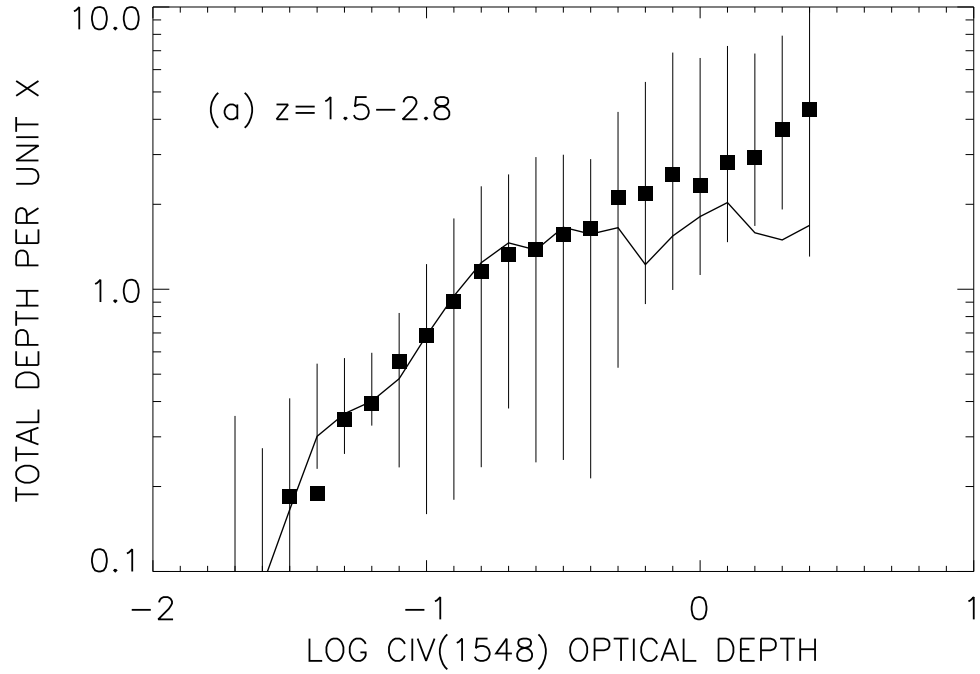


Fig. 18a.— Total absorption (the sum of the optical depths) per unit  $x$  in optical depth bins of 0.1. Each panel contains five quasars ordered by redshift. The results in (a) and (b) are based on HIRES data, and those in (c), (d) and (e) are based on ESI data. *Solid line*: distribution of the core sample. In (c), (d) and (e) this is smoothed to the ESI spectral resolution.

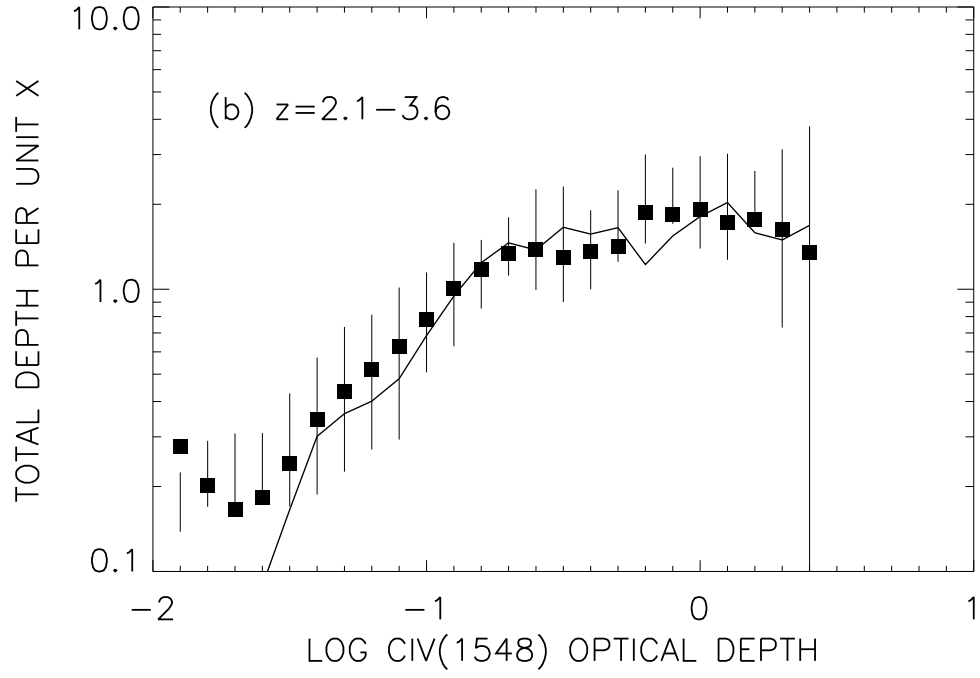


Fig. 18b.—

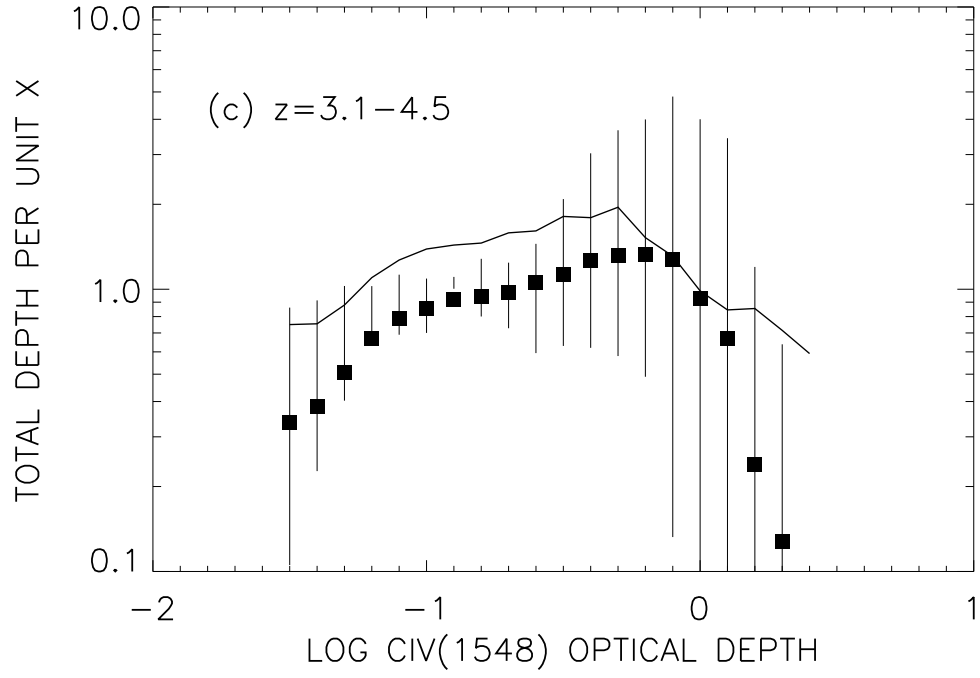


Fig. 18c.—

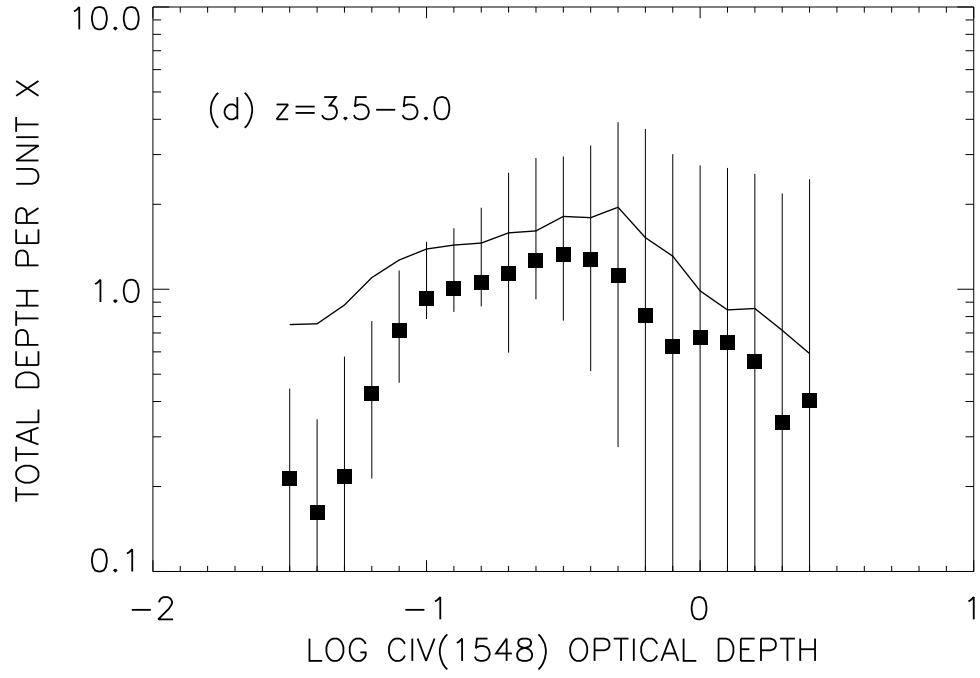


Fig. 18d.—

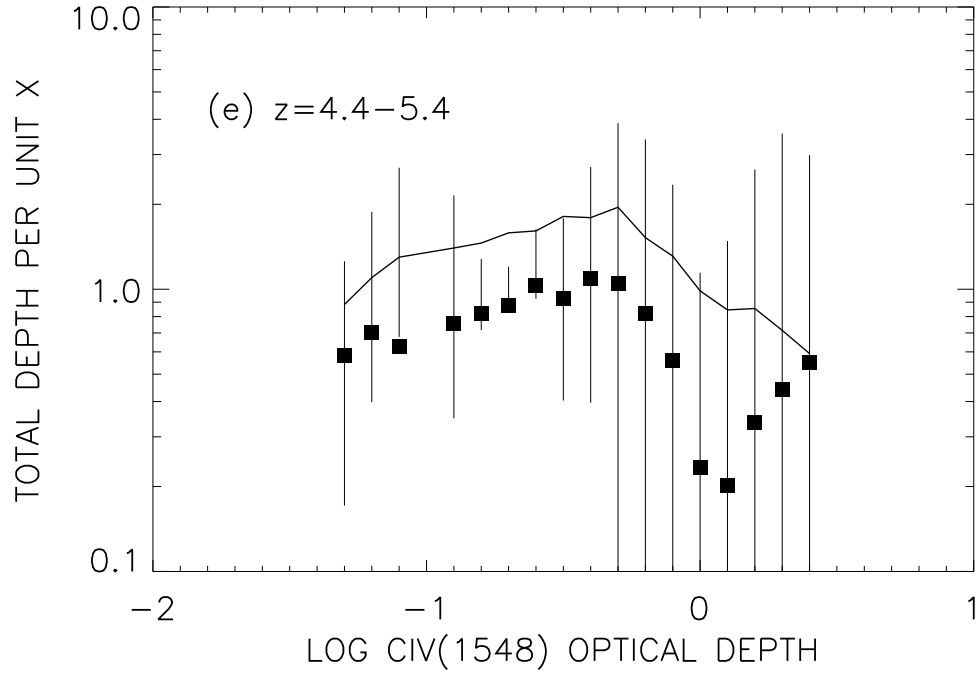


Fig. 18e.—